

Modelling of AC/DC Interactions of Converter-Interfaced Resources for Harmonic Power-Flow Studies in Microgrids

Johanna Kristin Maria Becker, *Student Member, IEEE*, Andreas Martin Kettner, *Member, IEEE*, Yihui Zuo, *Member, IEEE*, Federico Cecati, *Student Member, IEEE*, Sante Pugliese, *Member, IEEE*, Marco Liserre, *Fellow, IEEE*, and Mario Paolone, *Fellow, IEEE*

Abstract—Modern power distribution systems experience a large-scale integration of *Converter-Interfaced Distributed Energy Resources* (CIDERS). As acknowledged by recent literature, the interaction of individual CIDER components and different CIDERS through the grid can lead to undesirable amplification of harmonic frequencies. In order to analyze and mitigate such phenomenon the authors of this paper recently proposed a *Harmonic Power-Flow* (HPF) computation framework of polyphase grids with a high share of CIDERS. This paper extends this HPF framework to include the DC-side dynamics of CIDERS. The DC side is modelled by a controlled current source and the DC-link capacitor, and the AC/DC converter is represented by an average model. Including the latter into the CIDER model introduces a nonlinearity that needs to be approximated for the numerical solution of the HPF. The CIDER model and HPF framework are extended to include this linearization. The accuracy of the linearized CIDER model and the extended HPF framework is assessed for individual resources and a modified version of the CIGRÉ low-voltage benchmark microgrid. Namely, the spectra obtained from the HPF method are compared against time-domain simulations with Simulink. The observed maximum errors are $7.86\text{E-}5$ p.u. w.r.t. voltage magnitude, $3.1\text{E-}4$ p.u. w.r.t. current magnitude, and 22 mrad w.r.t. phase.

Index Terms—AC/DC interactions, converter-interfaced resources, DC-side modelling, distributed energy resources, harmonic power-flow study.

I. INTRODUCTION

MODERN power distribution systems host a large number of *Converter-Interfaced Distributed Energy Resources* (CIDERS), such as renewable generation, energy storage systems, and electric-vehicle charging stations. In such systems excessive harmonic distortion may occur [1] due to interactions between AC/DC converters and their components (i.e., DC-link capacitors, AC-side filters, and the associated controls). While the component sizes are tightly restricted by volume, weight, and cost [2], the controller design offers considerable freedom for mitigating such problems. For the

controller design process, it is crucial to understand the creation, propagation and coupling of harmonics due to the converter and AC/DC interactions.

In order to analyse the converter interactions through the grid, the authors of this paper recently proposed a generic and modular framework for the *Harmonic Power-Flow* (HPF) study of polyphase grids with a high share of CIDERS [3], [4]. The HPF method is based on polyphase circuit theory and *Linear Time-Periodic* (LTP) systems theory. More precisely, the HPF problem is formulated based on the closed-loop transfer functions of the CIDERS and the hybrid nodal equations of the grid. Notably, the CIDER model in [4] represents the AC-side components and their associated controllers in detail (incl. coupling between harmonics), but does not consider the DC side. For the study of the AC/DC interactions, the DC-side components and the corresponding controllers need to be included in the CIDER model.

In the recent past, the modelling of CIDERS for frequency ranges beyond the power-system fundamental component has been a prominent research topic. To this end, different levels of abstraction can be applied w.r.t. the DC-side model [5]. In reality, the DC side is typically composed of the following components (see Fig. 1a): a DC source, a DC/DC converter (e.g., a boost converter), and a DC-link capacitor connected to the AC/DC converter (e.g., [6]–[8]). However, this detailed model is unnecessarily complex for many studies. For most purposes, the dynamics of the DC source and the DC/DC converter can be neglected. In this case, as shown in Fig. 1b the elements are approximated by a current source, which emulates their aggregate behaviour (e.g., active power-point tracking). This representation is commonly used for harmonic analysis of individual CIDERS [9], [10] or an entire power system [11]. If the DC-link capacitor is sufficiently large (i.e., the DC-link ripples are negligible), the model can be simplified further. Namely, the entire DC side can be represented by a DC voltage source connected directly to the AC/DC converter (see Fig. 1c). This simplistic model is often used for impedance modelling and stability analysis of CIDERS [12], [13] and power grids [14].

This paper extends the aforementioned HPF framework proposed in [3], [4] to include the DC side of the CIDERS. Therefore, the extended HPF method is capable of analysing AC/DC interactions in addition to converter interactions through the grid. In this respect, the current-source model mentioned above is employed: i.e., the DC side is represented by a current source and a DC-link capacitor connected to the AC/DC converter. The latter introduces a nonlinearity into the model,

J. Becker, Y. Zuo and M. Paolone are with the Distributed Electrical Systems Laboratory at the École Polytechnique Fédérale de Lausanne (EPFL) in CH-1015 Lausanne, Switzerland (E-mail: {johanna.becker, yihui.zuo, mario.paolone}@epfl.ch).

A. Kettner is with PSI NEPLAN AG, 8700 Küsnacht, Switzerland (E-mail: andreas.kettner@neplan.ch).

F. Cecati, S. Pugliese and M. Liserre are with the Chair of Power Electronics at the Christian-Albrechts-Universität zu Kiel (CAU) in DE-24143 Kiel, Germany (E-mail: {fc, sapu, ml}@tf.uni-kiel.de).

This work was funded by the Schweizerischer Nationalfonds (SNF, Swiss National Science Foundation) via the National Research Programme NRP 70 “Energy Turnaround” (projects nr. 173661 and 197060) and by the Deutsche Forschungsgemeinschaft (DFG, German Research Foundation) via the Priority Programme DFG SPP 1984 “Hybrid and Multimodal Energy Systems” (project nr. 359982322).

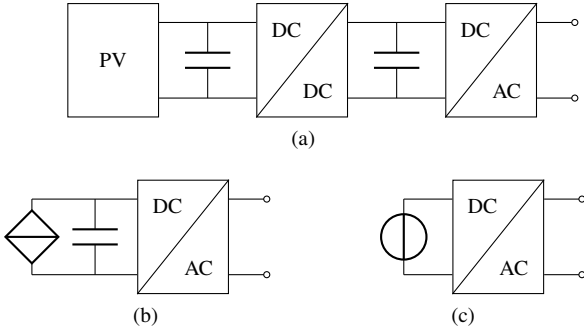


Fig. 1. Different approximations of the DC side of a CIDER. Detailed representation Fig. 1a, the current-source representation Fig. 1b and the voltage-source representation Fig. 1c.

which needs to be approximated for the numerical solution of the HPF problem. For this purpose, a suitable linearization is incorporated into the HPF algorithm. In this respect, the contributions of the paper are as follows. Firstly, the extended CIDER model which includes the DC side is presented and validated through time-domain simulations with Simulink. Secondly, the HPF framework is extended and applied to study a modified version of the CIGRÉ low-voltage benchmark microgrid.

The rest of this paper is organized as follows. Section II gives a generic description of the CIDER model including the linearization. Section III shows how the proposed description is incorporated into the HPF framework. The specific model of a grid-following CIDER including the DC-side dynamics is thoroughly illustrated in Section IV. Section V and Section VI show the validation of the extended framework for an individual resource and for an entire system, respectively. The conclusions are drawn in Section VII.

II. GENERIC MODEL OF THE CIDER

As mentioned in Section I, this paper extends the HPF framework proposed in [3], [4]. Unless otherwise stated, all hypotheses formulated in [3], [4] hold unchanged.

A. Primer on Linear Time-Periodic Systems

Harmonic analysis can be performed by means of *Linear Time-Periodic* (LTP) systems theory, which is a generalization of *Linear Time-Invariant* (LTI) systems theory [15]. This concept has recently been employed to analyze harmonics in power systems dominated by CIDERs (e.g., [3], [4], [16]).

Throughout this paper, all quantities are assumed to be time-periodic w.r.t. an underlying period T , which is the inverse of the fundamental frequency f_1 (i.e., $T = \frac{1}{f_1}$). As known from Fourier analysis, time-periodic quantities can be represented by a Fourier series

$$\mathbf{x}_n(t) = \sum_{h \in \mathcal{H}} \mathbf{X}_{n,h} \exp(jh2\pi f_1 t) \quad (1)$$

where $\mathbf{X}_{n,h} \in \mathbb{C}$ is the Fourier coefficient at the h -th harmonic of the fundamental frequency f_1 , with $h \in \mathcal{H} \subset \mathbb{Z}$.

As known, the multiplication of two signals in time domain results in a convolution of their spectra in frequency domain.

$$\mathbf{A}_n(t)\mathbf{x}_n(t) \leftrightarrow \mathbf{A}_n(f) * \mathbf{X}_n(f) = \hat{\mathbf{A}}_n \hat{\mathbf{X}}_n \quad (2)$$

where $\hat{\mathbf{A}}_n$ is the Toeplitz matrix of the Fourier coefficients $\mathbf{A}_{n,h}$, and $\hat{\mathbf{X}}_n$ is the column vector of the Fourier coefficients $\mathbf{X}_{n,h}$ [15]

$$\hat{\mathbf{A}}_n : \hat{\mathbf{A}}_{n,mk} = \mathbf{A}_{n,h}, \quad m, k \in \mathbb{N}, \quad h = m - k \in \mathcal{H} \quad (3)$$

$$\hat{\mathbf{X}}_n = \text{col}_{h \in \mathcal{H}}(\mathbf{X}_{n,h}) \quad (4)$$

B. Model of a CIDER Excluding the DC Side

In [3], the LTP models of the CIDERs are developed in the time domain. More precisely, a closed-loop model of the CIDER is derived based on the generic structure depicted in Fig. 2. It consists of the *power hardware* π and the *control software* κ , which are represented by LTP systems $\Sigma_{\pi,n}$ and $\Sigma_{\kappa,n}$, respectively, and the *reference calculation*, which is represented by a function $\mathbf{r}(\cdot, \cdot)$. $\Sigma_{\pi,n}$ and $\Sigma_{\kappa,n}$ jointly form the open-loop system Σ_n , which is described by

$$\Sigma_n : \begin{cases} \dot{\mathbf{x}}_n(t) = \mathbf{A}_n(t)\mathbf{x}_n(t) + \mathbf{B}_n(t)\mathbf{u}_n(t) + \mathbf{E}_n(t)\mathbf{w}_n(t) \\ \mathbf{y}_n(t) = \mathbf{C}_n(t)\mathbf{x}_n(t) + \mathbf{D}_n(t)\mathbf{u}_n(t) + \mathbf{F}_n(t)\mathbf{w}_n(t) \end{cases} \quad (5)$$

where $\mathbf{x}_n(t)$, $\mathbf{u}_n(t)$, $\mathbf{y}_n(t)$, and $\mathbf{w}_n(t)$ are the *state*, *input*, *output*, and *disturbance vector*, respectively. Accordingly, $\mathbf{A}_n(t)$, $\mathbf{B}_n(t)$, $\mathbf{C}_n(t)$, $\mathbf{D}_n(t)$, $\mathbf{E}_n(t)$, and $\mathbf{F}_n(t)$ are the *system*, *input*, *output*, *feed-through*, *input disturbance*, and *output disturbance matrix*, respectively.

As shown in Fig. 2, the power hardware $\Sigma_{\pi,n}$ and the control software $\Sigma_{\kappa,n}$ form a closed-loop system via the feedback matrix \mathbf{T}_n :

$$\mathbf{u}_n(t) = \mathbf{T}_n \mathbf{y}_n(t) \quad (6)$$

The internal response of the CIDER describes the behaviour of this closed-loop system:

Definition 1. *The internal response of the CIDER describes the relation from \mathbf{w}_n to \mathbf{y}_n . It is derived as the combination of the open-loop system Σ_n with the feedback matrix \mathbf{T}_n .*

Note that the feedback matrix describes the coordinate transformations which are applied to the measurements and control signals as they pass from the power hardware to the control software and vice versa. As explained in [3], the internal response is described in the harmonic domain by the following linear expression:

$$\hat{\mathbf{Y}}_n(\hat{\mathbf{W}}_n) = \hat{\mathbf{G}}_n \hat{\mathbf{W}}_n \quad (7)$$

where $\hat{\mathbf{Y}}_n$ and $\hat{\mathbf{W}}_n$ are the vectors of the Fourier coefficients of \mathbf{y}_n and \mathbf{w}_n in (5), respectively, and $\hat{\mathbf{G}}_n$ is the closed-loop gain of the CIDER derived in the harmonic domain.

The *grid response* additionally includes the reference calculation $\mathbf{r}(\cdot, \cdot)$ (i.e., grid-following or grid-forming control laws) as well as transformations $\mathbf{T}_{\kappa,\pi}$ (i.e., a change of coordinates between power hardware and control software) plus $\mathbf{T}_{\gamma,\pi}$ and $\mathbf{T}_{\pi,\gamma}$ (i.e., change of circuit configuration between grid and power hardware). Note that, as shown in Fig. 2, the grid-side quantities are the grid disturbance $\mathbf{w}_{\gamma,n}(t)$, the setpoint of the

CIDER $\mathbf{w}_{\sigma,n}(t)$, and the grid output $\mathbf{y}_{\gamma,n}(t)$ ¹ Accordingly, the grid response is defined as follows.

Definition 2. *The grid response of the CIDER describes the relation from $\mathbf{w}_{\gamma,n}$ and $\mathbf{w}_{\sigma,n}$ to $\mathbf{y}_{\gamma,n}$. It is derived through the combination of the internal response, the reference calculation $r(\cdot, \cdot)$ and the grid-side transformations $\mathbf{T}_{\pi|\gamma,n}$ and $\mathbf{T}_{\gamma|\pi,n}$.*

As shown in [3], the grid response can be expressed in the harmonic domain as:

$$\hat{\mathbf{Y}}_{\gamma,n}(\hat{\mathbf{W}}_{\gamma,n}, \hat{\mathbf{W}}_{\sigma,n}) = \hat{\mathbf{T}}_{\gamma|\pi,n} \hat{\mathbf{Y}}_{\pi,n}(\underbrace{\hat{\mathbf{T}}_{\pi|\gamma,n} \hat{\mathbf{W}}_{\gamma,n}}_{\hat{\mathbf{W}}_{\pi,n}}, \hat{\mathbf{W}}_{\sigma,n}) \quad (8)$$

Regarding the function $\hat{\mathbf{Y}}_{\pi,n}(\cdot, \cdot)$, note in Fig. 2 and recall from (7) that the mapping from $\hat{\mathbf{W}}_{\pi,n}$ to $\hat{\mathbf{Y}}_{\pi,n}$ is linear. Indeed, this is why the gain $\hat{\mathbf{G}}_n$ can be calculated analytically. By contrast, the mapping from $\hat{\mathbf{W}}_{\sigma,n}$ to $\hat{\mathbf{Y}}_{\pi,n}$ includes the reference calculation, which may be nonlinear. However, since this potential nonlinearity is not part of the closed-loop structure, it does not necessitate any linearization (see [3]).

C. Model of a CIDER Including the DC Side

In the HPF framework proposed in [3], [4] the CIDER model covers only the AC-side components. That is, the AC/DC converter and DC side are represented by a controlled AC voltage source. Since the parts of the model related to the internal response are all linear, they can be represented by LTP models without further approximations. Notably, one can use Eq. (7) to find the internal response of a generic CIDER, which is characterized by the closed-loop gain $\hat{\mathbf{G}}_n$.

If the DC side of the CIDER shall be analyzed in detail, the DC-side components as well as the AC/DC converter need to be included in the HPF model. The latter introduces a nonlinearity into the model. As will be shown shortly, this is due to the power balance equation used in the average model of the converter. Due to the aforementioned nonlinearity, it is in general not possible to find an explicit solution for the internal response because the equations describing the closed-loop system cannot be solved analytically. However, one can locally approximate the internal response through linearization w.r.t. the operating point and apply the same methodology as before. The operating point needs to be explicitly considered as a variable in the linearized version of the open-loop model (5) for the numerical solution of the HPF problem.

Let $\mathbf{y}_{o,n}(t)$ denote the operating point. Via linearization w.r.t. the operating point, one obtains a model that is analogous to (5), in which $\mathbf{y}_{o,n}(t)$ appears as an additional variable:

$$\mathbf{A}_n : \mathbf{A}_n(t, \mathbf{y}_{o,n}(t)), \mathbf{B}_n \text{ etc. analogous} \quad (9)$$

In order to facilitate the formulation and solution of the HPF problem, the following decomposition is proposed:

$$\mathbf{A}_n(t, \mathbf{y}_{o,n}(t)) = \tilde{\mathbf{A}}_n(t) + \bar{\mathbf{A}}_n(t, \mathbf{y}_{o,n}(t)) \quad (10)$$

¹For a grid-following CIDER, the grid disturbance is the nodal voltage and the grid output is the injected current. For a grid-forming CIDER, the grid disturbance is the injected current and the grid output is the nodal voltage.

That is, the matrices can be separated into a term $\tilde{\mathbf{A}}_n$ which is invariant w.r.t. the operating point, and another term $\bar{\mathbf{A}}_n$ which is a function of it. By consequence, in case the operating point changes, only the second term needs to be recalculated.

Based on the linearized open-loop CIDER model, one can derive the closed-loop model both in time and frequency domain. In doing so, keep in mind that the associated matrices in time and frequency domain are functions of $\mathbf{y}_{o,n}(t)$ and $\hat{\mathbf{Y}}_{o,n}$, respectively. The same applies to the internal and grid response. The closed-loop gain which characterizes the internal response is of the form (cf. (7))

$$\hat{\mathbf{Y}}_n(\hat{\mathbf{W}}_n, \hat{\mathbf{Y}}_{o,n}) = \hat{\mathbf{G}}_n(\hat{\mathbf{Y}}_{o,n}) \hat{\mathbf{W}}_n \quad (11)$$

Analogously, the grid response is written as follows (cf. (8)):

$$\begin{aligned} \hat{\mathbf{Y}}_{\gamma,n}(\hat{\mathbf{W}}_{\gamma,n}, \hat{\mathbf{W}}_{\sigma,n}, \hat{\mathbf{Y}}_{o,n}) \\ = \hat{\mathbf{T}}_{\gamma|\pi,n} \hat{\mathbf{Y}}_{\pi,n}(\underbrace{\hat{\mathbf{T}}_{\pi|\gamma,n} \hat{\mathbf{W}}_{\gamma,n}}_{\hat{\mathbf{W}}_{\pi,n}}, \hat{\mathbf{W}}_{\sigma,n}, \hat{\mathbf{Y}}_{o,n}) \end{aligned} \quad (12)$$

Without loss of generality, it is assumed that the operating point is a subset of the output vector of the internal response:

$$\mathbf{y}_{o,n}(t) \subset \mathbf{y}_n(t) \quad (13)$$

Note that, when defining the open-loop model of the CIDER, any block of the vectors \mathbf{x} , \mathbf{u} , and \mathbf{w} can be included in the output equation if needed. Accordingly, there exists a matrix $\mathbf{T}_{o,n}$ such that

$$\mathbf{y}_{o,n}(t) = \mathbf{T}_{o,n} \mathbf{y}_n(t) \quad (14)$$

Respectively, in the harmonic domain

$$\hat{\mathbf{Y}}_{o,n} = \hat{\mathbf{T}}_{o,n} \hat{\mathbf{Y}}_n \quad (15)$$

This definition will be used later in the formulation of the Newton-Raphson method for solving the HPF problem.

III. EXTENSION OF THE SOLUTION ALGORITHM FOR THE HARMONIC POWER-FLOW PROBLEM

In the HPF framework proposed in [3], the power system is described by two sets of nodal equations, which are formulated from the point of view of the grid and the resources, respectively. In this respect, the unknowns are taken to be the nodal injected currents $\hat{\mathbf{I}}_S$ at the nodes S with grid-forming CIDERs and the nodal phase-to-ground voltages $\hat{\mathbf{V}}_R$ at the nodes R with grid-following CIDERs.

From the point of view of the grid, the nodal equations are formulated using hybrid parameters:

$$\hat{\mathbf{V}}_S(\hat{\mathbf{I}}_S, \hat{\mathbf{V}}_R) = \hat{\mathbf{H}}_{S \times S} \hat{\mathbf{I}}_S + \hat{\mathbf{H}}_{S \times R} \hat{\mathbf{V}}_R \quad (16)$$

$$\hat{\mathbf{I}}_R(\hat{\mathbf{I}}_S, \hat{\mathbf{V}}_R) = \hat{\mathbf{H}}_{R \times S} \hat{\mathbf{I}}_S + \hat{\mathbf{H}}_{R \times R} \hat{\mathbf{V}}_R \quad (17)$$

where $\hat{\mathbf{H}}_{S \times S}$, $\hat{\mathbf{H}}_{S \times R}$, $\hat{\mathbf{H}}_{R \times S}$ and $\hat{\mathbf{H}}_{R \times R}$ are the blocks of the hybrid matrix $\hat{\mathbf{H}}$ associated with S and R .

From the point of view of the CIDERs, the nodal equations are described by the grid responses:

$$\begin{aligned} s \in S : \quad \hat{\mathbf{V}}_s(\hat{\mathbf{I}}_s, V_{\sigma,s}, f_{\sigma,s}, \hat{\mathbf{Y}}_{o,s}) \\ = \hat{\mathbf{Y}}_{\gamma,s}(\hat{\mathbf{I}}_s, V_{\sigma,s}, f_{\sigma,s}, \hat{\mathbf{Y}}_{o,s}) \end{aligned} \quad (18)$$

$$r \in R : \quad \hat{\mathbf{I}}_r(\hat{\mathbf{V}}_r, S_{\sigma,r}, \hat{\mathbf{Y}}_{o,r}) = \hat{\mathbf{Y}}_{\gamma,r}(\hat{\mathbf{V}}_r, S_{\sigma,r}, \hat{\mathbf{Y}}_{o,r}) \quad (19)$$

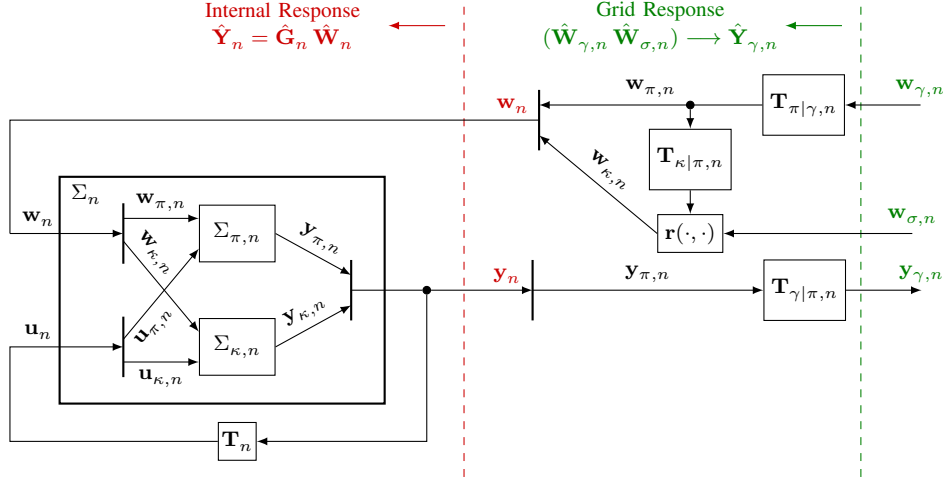


Fig. 2. General structure of a CIDER. The power hardware $\Sigma_{\pi,n}$ and control software $\Sigma_{\kappa,n}$ form the open-loop system Σ_n . The internal response is derived by closing the loop through the feedback matrix T_n (see (7)). The grid response additionally includes the reference calculation $r(\cdot, \cdot)$ and the required transformation matrices (see (12)). The transformation matrix $T_{\kappa|\pi,n}$ represents a change of coordinates between power hardware and control software. $T_{\pi|\gamma,n}$ and $T_{\gamma|\pi,n}$ represent a change of coordinates or circuit configuration between grid and power hardware.

Note that grid-forming CIDERs take voltage and frequency as setpoints (i.e., $V_{\sigma,s}$ and $f_{\sigma,s}$), and grid-following CIDERs active and reactive powers (i.e., $S_{\sigma,r} = P_{\sigma,r} + jQ_{\sigma,r}$).

In equilibrium, the mismatch equations between (16)–(17) and (18)–(19) must be zero (i.e., they yield identical results):

$$\Delta \hat{V}_S(\hat{I}_S, \hat{V}_R, \mathbf{V}_\sigma, \mathbf{f}_\sigma, \hat{Y}_{o,S}) = \mathbf{0} \quad (20)$$

$$\Delta \hat{I}_R(\hat{I}_S, \hat{V}_R, \mathbf{S}_\sigma, \hat{Y}_{o,R}) = \mathbf{0} \quad (21)$$

where \mathbf{V}_σ , \mathbf{f}_σ , and \mathbf{S}_σ are column vectors built of the setpoints $V_{\sigma,s}$, $f_{\sigma,s}$ ($s \in S$) and $S_{\sigma,r}$ ($r \in R$), respectively. This system of equations can be solved by means of the Newton-Raphson method.

As known from numerical analysis, the Newton-Raphson method requires the calculation (and inversion) of a Jacobian matrix $\hat{\mathbf{J}}$, which is computationally intensive. In the original HPF framework proposed in [3], most blocks of the Jacobian matrix are constant, because the grid equations (16)–(17) are exactly linear, and the CIDER responses (8) are linear except for the reference calculation. In the extended formulation (20)–(21) of the HPF problem, the operating points $\hat{Y}_{o,S}$ and $\hat{Y}_{o,R}$ of the CIDERs appear as additional unknowns. Therefore, the entire Jacobian matrix has to be recalculated in each iteration of the Newton-Raphson method. In doing so, the fact that the operating points are a subset of the internal responses – as postulated in (15) – needs to be taken into account. As a result, one obtains the extended Newton-Raphson algorithm which is shown in Algorithm 1. The differences w.r.t. to the original method are highlighted in blue.

Like the unknowns related to the grid (i.e., \hat{V}_S and \hat{I}_R), the operating points of the CIDERs (i.e., $\hat{Y}_{o,S}$ and $\hat{Y}_{o,R}$) need to be initialized at the start (see Lines 3 and 4 and Lines 5 and 6 of Algorithm 1, respectively), and then updated during each iteration. For the initialization, one can make an “educated guess” based on the fact that the operating points are AC and DC quantities (i.e., voltages and currents). AC quantities are initialized assuming balanced, sinusoidal conditions (i.e., only

a positive-sequence component at the fundamental tone) and using nominal values (e.g., magnitude 1 p.u. and angle 0 rad for voltages) or setpoints. This is known as “flat start”. DC quantities are initialized assuming ideal steady-state conditions (i.e., a constant value only) and using nominal values or setpoints. For the update, equation (15) is used: that is, the operating points are retrieved from the CIDERs via the output equations (see Lines 20 and 21 of Algorithm 1).

IV. GRID-FOLLOWING CIDER INCLUDING THE DC-SIDE

In this section, the detailed model of a grid-following CIDER including the DC-side dynamics is developed. Specifically, a CIDER with DC-voltage control is considered. To this end, the DC side is represented by the current-source model as introduced in Section I and Fig. 1b. The precise structure of the CIDER is shown in Fig. 3. The power hardware consists of an *LCL* filter on the AC side, plus a current source and a link capacitor on the DC side. The control software is composed of a cascade of controllers. For the sake of illustration, PI controllers are considered. Note that the measurements and control signals, that are exchanged between the power hardware and control software, pass through coordinate transformations. In this particular case, the Park transform is employed (this is common for three-phase CIDERs). The reference calculation computes the current setpoint for the control software based on the power setpoint and the voltage at the point of connection.

A. Power Hardware

In the frequency range of interest for HPF studies, the fast dynamics of the DC source and the DC/DC converter can be neglected. Therefore, by assuming that the load is of constant-power type, the DC equivalent may be described by a controlled current source.

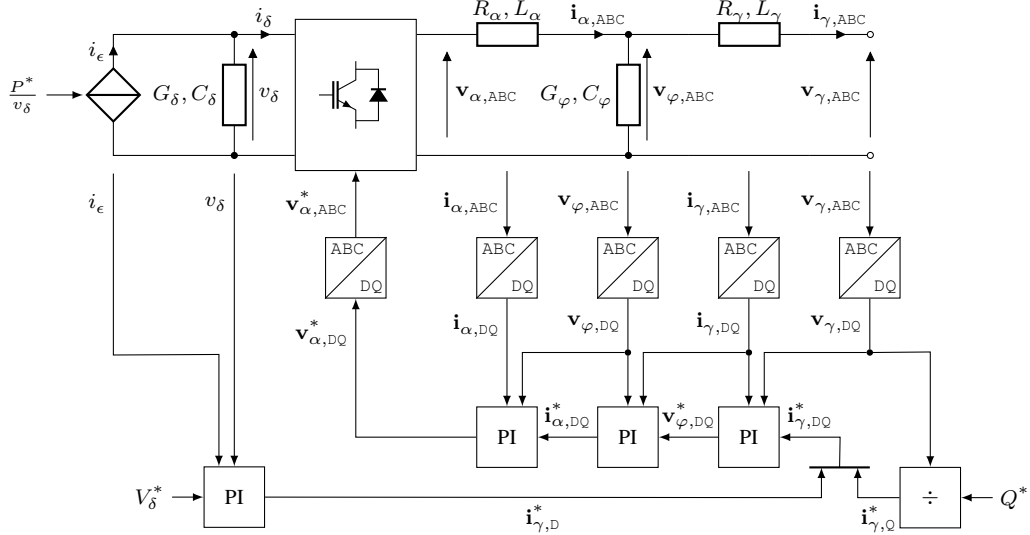


Fig. 3. Overview of the grid-following CIDER including DC-side dynamics. The power hardware is connected through measurements and coordinate transformations (i.e., in case of AC signals) to the control software.

Algorithm 1 Newton-Raphson solution of the HPF problem.

```

1: procedure HPF( $\Delta \hat{\mathbf{V}}_S(\cdot, \cdot, \cdot)$ ,  $\Delta \hat{\mathbf{I}}_R(\cdot, \cdot, \cdot)$ ,  $\mathbf{V}_\sigma$ ,  $\mathbf{f}_\sigma$ ,  $\mathbf{S}_\sigma$ )
2:   # Initialization
3:    $\hat{\mathbf{I}}_S \leftarrow \mathbf{0}$ 
4:    $\hat{\mathbf{V}}_R \leftarrow \text{flat\_start}()$ 
5:    $\hat{\mathbf{Y}}_{o,S} \leftarrow \text{initialize\_operating\_point}()$ 
6:    $\hat{\mathbf{Y}}_{o,R} \leftarrow \text{initialize\_operating\_point}()$ 
7:   while  $\max(|\Delta \hat{\mathbf{V}}_S|, |\Delta \hat{\mathbf{I}}_R|) \geq \epsilon$  do
8:     # Residuals
9:      $\Delta \hat{\mathbf{V}}_S \leftarrow \Delta \hat{\mathbf{V}}_S(\hat{\mathbf{I}}_S, \hat{\mathbf{V}}_R, \mathbf{V}_\sigma, \mathbf{f}_\sigma, \hat{\mathbf{Y}}_{o,S})$ 
10:     $\Delta \hat{\mathbf{I}}_R \leftarrow \Delta \hat{\mathbf{I}}_R(\hat{\mathbf{I}}_S, \hat{\mathbf{V}}_R, \mathbf{S}_\sigma, \hat{\mathbf{Y}}_{o,R})$ 
11:    # Jacobian matrix
12:     $\hat{\mathbf{J}}_{S \times S} \leftarrow \partial_S \Delta \hat{\mathbf{V}}_S(\hat{\mathbf{I}}_S, \hat{\mathbf{V}}_R, \mathbf{V}_\sigma, \mathbf{f}_\sigma, \hat{\mathbf{Y}}_{o,S})$ 
13:     $\hat{\mathbf{J}}_{S \times R} \leftarrow \partial_R \Delta \hat{\mathbf{V}}_S(\hat{\mathbf{I}}_S, \hat{\mathbf{V}}_R, \mathbf{V}_\sigma, \mathbf{f}_\sigma, \hat{\mathbf{Y}}_{o,S})$ 
14:     $\hat{\mathbf{J}}_{R \times S} \leftarrow \partial_S \Delta \hat{\mathbf{I}}_R(\hat{\mathbf{I}}_S, \hat{\mathbf{V}}_R, \mathbf{S}_\sigma, \hat{\mathbf{Y}}_{o,R})$ 
15:     $\hat{\mathbf{J}}_{R \times R} \leftarrow \partial_R \Delta \hat{\mathbf{I}}_R(\hat{\mathbf{I}}_S, \hat{\mathbf{V}}_R, \mathbf{S}_\sigma, \hat{\mathbf{Y}}_{o,R})$ 
16:    # Newton-Raphson iteration
17:     $\begin{bmatrix} \Delta \hat{\mathbf{I}}_S \\ \Delta \hat{\mathbf{V}}_R \end{bmatrix} \leftarrow \begin{bmatrix} \hat{\mathbf{J}}_{S \times S} & \hat{\mathbf{J}}_{S \times R} \\ \hat{\mathbf{J}}_{R \times S} & \hat{\mathbf{J}}_{R \times R} \end{bmatrix}^{-1} \begin{bmatrix} \Delta \hat{\mathbf{V}}_S \\ \Delta \hat{\mathbf{I}}_R \end{bmatrix}$ 
18:     $\begin{bmatrix} \hat{\mathbf{I}}_S \\ \hat{\mathbf{V}}_R \end{bmatrix} \leftarrow \begin{bmatrix} \hat{\mathbf{I}}_S \\ \hat{\mathbf{V}}_R \end{bmatrix} - \begin{bmatrix} \Delta \hat{\mathbf{I}}_S \\ \Delta \hat{\mathbf{V}}_R \end{bmatrix}$ 
19:    # Update
20:     $\hat{\mathbf{Y}}_{o,S} \leftarrow \hat{\mathbf{T}}_{o,S} \hat{\mathbf{Y}}_S \forall s \in \mathcal{S}$ 
21:     $\hat{\mathbf{Y}}_{o,R} \leftarrow \hat{\mathbf{T}}_{o,R} \hat{\mathbf{Y}}_R \forall r \in \mathcal{R}$ 
22:  end while
23: end procedure

```

Hypothesis 1. The DC equivalent current i_ϵ is computed in order to track the power setpoint P^* using the DC-side voltage v_δ :

$$i_\epsilon(t) = \frac{P^*}{v_\delta(t)} \quad (22)$$

In general, it can be assumed that the DC-side voltage control

loop of the CIDER is designed to track its reference (e.g., a well-tuned PI controller). Namely, in steady-state its DC component $V_{\delta,0}$ follows the reference V_δ^* .

Hypothesis 2. The DC-voltage control tracks the DC-voltage reference in the DC component without steady-state error. That is,:

$$V_{\delta,0} = V_\delta^* \quad (23)$$

Typically, the DC-voltage harmonics are negligible when compared to the DC component. The following assumption is made.

Hypothesis 3. The time-variant signal content of $v_\delta(t)$, as given by $\xi(t)$ below, is low.

$$v_\delta(t) = V_{\delta,0}(1 + \xi(t)), \quad |\xi(t)| \ll 1 \quad (24)$$

As a consequence of Hyp. 2 and Hyp. 3, (22) can be linearized around the DC voltage reference V_δ^* .

$$i_\epsilon(t) \approx \frac{P^*}{V_\delta^*} - \frac{P^*}{V_\delta^{*2}}(v_\delta(t) - V_\delta^*) \quad (25)$$

$$= 2 \frac{P^*}{V_\delta^*} - \frac{P^*}{V_\delta^{*2}} v_\delta(t) \quad (26)$$

Typically, the actuator is a *Pulse-Width Modulator* (PWM). Assuming that the PWM has a high switching frequency (i.e., beyond the range of frequencies which are of interest for HPF analysis), these high-frequency components do not need to be considered. Thus, the actuator can be represented by an *average model*.

Hypothesis 4. In the frequency range of interest for the HPF study, the switching losses and high-frequency components due to the converter switching are negligible. Therefore, the converter can be represented by an average model based on the instantaneous power balance equation between the DC-side power P_δ and the AC-side power P_α .

$$P_\delta = P_\alpha \quad (27)$$

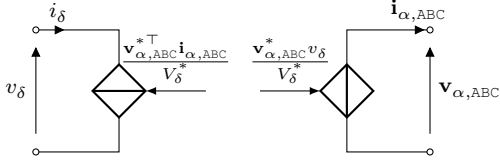


Fig. 4. Representation of the actuator by an average model, consisting of a controlled current source on the DC side and a controlled voltage source on the AC side.

The average model consists of a controlled current source on the DC side and a controlled voltage source on the AC side [17] (see Fig. 4). The AC-side voltage is derived from the AC-side reference voltage $\mathbf{v}_{\alpha,ABC}^*$ and the DC-side voltage v_δ through:

$$\mathbf{v}_{\alpha,ABC}(t) = \frac{1}{V_\delta^*} \mathbf{v}_{\alpha,ABC}^*(t) v_\delta(t) \quad (28)$$

The DC-side current i_δ is derived from $\mathbf{v}_{\alpha,ABC}^*$ and the AC-side actuator current $\mathbf{i}_{\alpha,ABC}$:

$$i_\delta(t) = \frac{1}{V_\delta^*} \sum_{j=ABC} v_{\alpha,j}^*(t) i_{\alpha,j}(t) = \frac{1}{V_\delta^*} \mathbf{v}_{\alpha,ABC}^{*\top}(t) \mathbf{i}_{\alpha,ABC}(t) \quad (29)$$

As previously mentioned in Section II-C, these equations are nonlinear w.r.t. the point of view of the state-space variables. Therefore, as proposed in Section II-C, the actuator model is linearized around the operating point

$$\mathbf{y}_o(t) = \begin{bmatrix} \bar{\mathbf{v}}_{\alpha,ABC}^*(t) \\ \bar{\mathbf{i}}_{\alpha,ABC}(t) \\ \bar{v}_\delta(t) \end{bmatrix} \quad (30)$$

which leads to the following linear representation (i.e., a Taylor expansion of (28) and (29) around (30) truncated at the first term):

$$\mathbf{v}_{\alpha,ABC}(t) \approx \frac{1}{V_\delta^*} \left(\bar{\mathbf{v}}_{\alpha,ABC}^*(t) v_\delta(t) + \bar{v}_\delta(t) \mathbf{v}_{\alpha,ABC}^*(t) - \bar{v}_\delta(t) \bar{\mathbf{v}}_{\alpha,ABC}^*(t) \right) \quad (31)$$

$$i_\delta(t) \approx \frac{1}{V_\delta^*} \left(\bar{\mathbf{v}}_{\alpha,ABC}^{*\top}(t) \mathbf{i}_{\alpha,ABC}(t) + \bar{\mathbf{i}}_{\alpha,ABC}^\top(t) \mathbf{v}_{\alpha,ABC}^*(t) - \bar{\mathbf{i}}_{\alpha,ABC}^\top(t) \bar{\mathbf{v}}_{\alpha,ABC}^*(t) \right) \quad (32)$$

Note that all quantities are linear time-periodic and thus the expression can be employed when deriving the LTP model of the power hardware.

A general derivation of the filter equations was described by the authors of this paper in [4]. An inductive and capacitive filter stage are described by the following differential equations, respectively:

$$\mathbf{v}_{\lambda-1,ABC} - \mathbf{v}_{\lambda+1,ABC} = \mathbf{R}_{\lambda,ABC} \mathbf{i}_{\lambda,ABC} + \mathbf{L}_{\lambda,ABC} \frac{d}{dt} \mathbf{i}_{\lambda,ABC} \quad (33)$$

$$\mathbf{i}_{\lambda-1,ABC} - \mathbf{i}_{\lambda+1,ABC} = \mathbf{G}_{\lambda,ABC} \mathbf{v}_{\lambda,ABC} + \mathbf{C}_{\lambda,ABC} \frac{d}{dt} \mathbf{v}_{\lambda,ABC} \quad (34)$$

$\mathbf{R}_{\lambda,ABC}$, $\mathbf{L}_{\lambda,ABC}$ and $\mathbf{G}_{\lambda,ABC}$, $\mathbf{C}_{\lambda,ABC}$ are the compound electrical parameters of the inductive and capacitive filter stage, respectively. $\mathbf{i}_{\lambda,ABC}$ is the current flowing through the inductive

filter stage, and $\mathbf{v}_{\lambda-1,ABC}$, $\mathbf{v}_{\lambda+1,ABC}$ are the voltages at the start and end node of that stage, respectively. Similarly, $v_{\lambda,\pi}$ is the voltage across the capacitive filter stage, and $\mathbf{i}_{\lambda-1,\pi}$, $\mathbf{i}_{\lambda+1,\pi}$ are the currents flowing into and out of it, respectively.

To obtain the state-space model of the power hardware, the equations of the AC and the DC filter stages are combined with the linearized actuator model and the current of the DC equivalent. More precisely, one needs to insert (31) and (32) as well as (26) into the equations of the filter stages and, then, derive the state-space format.

Thus, the state of the combined power hardware is given by the inductor currents $\mathbf{i}_{\alpha,ABC}$ and $\mathbf{i}_{\gamma,ABC}$ and the capacitor voltage $\mathbf{v}_{\varphi,ABC}$ on the AC side and the capacitor voltage v_δ on the DC side. The input is the actuator voltage reference $\mathbf{v}_{\alpha,ABC}^*$. The disturbances are the grid voltage $\mathbf{v}_{\gamma,ABC}$, the average DC-side equivalent current described by $\frac{P^*}{V_\delta^*}$ and the operating point of the actuator voltage reference $\bar{\mathbf{v}}_{\alpha,ABC}^*$. The output includes the state and the grid voltage as well as the DC-side equivalent current i_ϵ . Namely,

$$\mathbf{x}_\pi(t) = \begin{bmatrix} \mathbf{i}_{\alpha,ABC}(t) \\ \mathbf{v}_{\varphi,ABC}(t) \\ \mathbf{i}_{\gamma,ABC}(t) \\ v_\delta(t) \end{bmatrix} \quad (35)$$

$$\mathbf{u}_\pi(t) = \mathbf{v}_{\alpha,ABC}^*(t) \quad (36)$$

$$\mathbf{w}_\pi(t) = \begin{bmatrix} \mathbf{v}_{\gamma,ABC}(t) \\ \frac{P^*}{V_\delta^*} \\ \bar{\mathbf{v}}_{\alpha,ABC}^*(t) \end{bmatrix} \quad (37)$$

$$\mathbf{y}_\pi(t) = \begin{bmatrix} \mathbf{x}_\pi(t) \\ \mathbf{v}_{\gamma,ABC}(t) \\ i_\epsilon(t) \end{bmatrix} \quad (38)$$

As one can see from (31) and (32) the third term is bilinear w.r.t. the components of the operating point (i.e., $\bar{v}_\delta \bar{\mathbf{v}}_{\alpha,ABC}^*$ and $\bar{\mathbf{i}}_{\alpha,ABC}^\top \bar{\mathbf{v}}_{\alpha,ABC}^*$). In order to put this in the form of an LTP system, one of the quantities (i.e., the voltage reference $\bar{\mathbf{v}}_{\alpha,ABC}^*$) is added to the disturbance vector, while \bar{v}_δ and $\bar{\mathbf{i}}_{\alpha,ABC}^\top$ enter the matrices. Similarly, the first term of (26) (i.e., $\frac{P^*}{V_\delta^*}$) is defined as a disturbance to the state-space model.

Recall that the matrices can be separated in two terms: one being invariant w.r.t. the operating point and one being a function of it.

$$\mathbf{A}_\pi(t) = \tilde{\mathbf{A}}_\pi(t) + \bar{\mathbf{A}}_\pi(t, \mathbf{y}_{o,n}(t)) \quad (39)$$

Each of these matrices itself can be described by its Fourier coefficients as in (1). The matrices of the state-space model that are invariant w.r.t. the operating point are given by

$$\tilde{\mathbf{A}}_{\pi,0} = \begin{bmatrix} -\mathbf{L}_\alpha^{-1} \mathbf{R}_\alpha & -\mathbf{L}_\alpha^{-1} & \mathbf{0}_{3 \times 3} & \mathbf{0}_{3 \times 1} \\ \mathbf{C}_\varphi^{-1} & -\mathbf{C}_\varphi^{-1} \mathbf{G}_\varphi & -\mathbf{C}_\varphi^{-1} & \mathbf{0}_{3 \times 1} \\ \mathbf{0}_{3 \times 3} & \mathbf{L}_\gamma^{-1} & -\mathbf{L}_\gamma^{-1} \mathbf{R}_\gamma & \mathbf{0}_{3 \times 1} \\ \mathbf{0}_{1 \times 3} & \mathbf{0}_{1 \times 3} & \mathbf{0}_{1 \times 3} & (\tilde{\mathbf{A}}_{\pi,0})_{44} \end{bmatrix} \quad (40)$$

$$(\tilde{\mathbf{A}}_{\pi,0})_{44} = -C_\delta^{-1} G_\delta - C_\delta^{-1} \frac{P^*}{V_\delta^{*2}} \quad (41)$$

$$\tilde{\mathbf{B}}_{\pi,0} = \mathbf{0}_{10 \times 3} \quad (42)$$

$$\tilde{\mathbf{E}}_{\pi,0} = \begin{bmatrix} \mathbf{0}_{6 \times 3} & \mathbf{0}_{6 \times 1} & \mathbf{0}_{6 \times 3} \\ -\mathbf{L}_\gamma^{-1} & \mathbf{0}_{3 \times 1} & \mathbf{0}_{3 \times 3} \\ \mathbf{0}_{1 \times 3} & -2C_\delta^{-1} & \mathbf{0}_{1 \times 3} \end{bmatrix} \quad (43)$$

$$\tilde{\mathbf{C}}_{\pi,0} = \begin{bmatrix} \text{diag}(\mathbf{1}_9) & \mathbf{0}_{9 \times 1} \\ \mathbf{0}_{1 \times 9} & 1 \\ \mathbf{0}_{3 \times 9} & \mathbf{0}_{3 \times 1} \\ \mathbf{0}_{1 \times 9} & -\frac{P^*}{V_\delta^*} \end{bmatrix} \quad (44)$$

$$\tilde{\mathbf{D}}_{\pi,0} = \mathbf{0}_{14 \times 3} \quad (45)$$

$$\tilde{\mathbf{F}}_{\pi,0} = \begin{bmatrix} \mathbf{0}_{10 \times 3} & \mathbf{0}_{10 \times 1} & \mathbf{0}_{10 \times 3} \\ \text{diag}(\mathbf{1}_3) & \mathbf{0}_{3 \times 1} & \mathbf{0}_{3 \times 3} \\ \mathbf{0}_{1 \times 3} & 2 & \mathbf{0}_{1 \times 3} \end{bmatrix} \quad (46)$$

and all other Fourier coefficients equal to zero. The matrices that are a function of the operating point are given by

$$\bar{\mathbf{A}}_{\pi,h} = \begin{bmatrix} \mathbf{0}_{3 \times 3} & \mathbf{0}_{3 \times 6} & (\bar{\mathbf{A}}_{\pi,h})_{13} \\ \mathbf{0}_{6 \times 3} & \mathbf{0}_{6 \times 6} & \mathbf{0}_{6 \times 1} \\ (\bar{\mathbf{A}}_{\pi,h})_{31} & \mathbf{0}_{1 \times 6} & 0 \end{bmatrix} \quad (47)$$

$$(\bar{\mathbf{A}}_{\pi,h})_{13} = \frac{1}{V_\delta^*} \mathbf{L}_\alpha^{-1} \bar{\mathbf{V}}_{\alpha,ABC,h}^* \quad (48)$$

$$(\bar{\mathbf{A}}_{\pi,h})_{31} = -\frac{1}{V_\delta^*} C_\delta^{-1} \bar{\mathbf{V}}_{\alpha,ABC,h}^{*\top} \quad (49)$$

$$\bar{\mathbf{B}}_{\pi,h} = \begin{bmatrix} \frac{1}{V_\delta^*} \mathbf{L}_\alpha^{-1} \bar{V}_{\delta,h} \\ \mathbf{0}_{6 \times 3} \\ -\frac{1}{V_\delta^*} C_\delta^{-1} \bar{\mathbf{I}}_{\alpha,ABC,h}^\top \end{bmatrix} \quad (50)$$

$$\bar{\mathbf{E}}_{\pi,h} = \begin{bmatrix} \mathbf{0}_{3 \times 4} & -\frac{1}{V_\delta^*} \mathbf{L}_\alpha^{-1} \bar{V}_{\delta,h} \\ \mathbf{0}_{3 \times 4} & \mathbf{0}_{3 \times 3} \\ \mathbf{0}_{3 \times 4} & \mathbf{0}_{3 \times 3} \\ \mathbf{0}_{1 \times 4} & \frac{1}{V_\delta^*} C_\delta^{-1} \bar{\mathbf{I}}_{\alpha,ABC,h}^\top \end{bmatrix} \quad (51)$$

$$\bar{\mathbf{C}}_{\pi,h} = \mathbf{0}_{14 \times 10} \quad (52)$$

$$\bar{\mathbf{D}}_{\pi,h} = \mathbf{0}_{14 \times 3} \quad (53)$$

$$\bar{\mathbf{F}}_{\pi,h} = \mathbf{0}_{14 \times 7} \quad (54)$$

B. Control Software

The state-space model of the control software is obtained employing the theory described in [4]. The DC-side controller provides the reference for the DC current i_δ^* , which is used for the grid current reference in the D-component $i_{\gamma,D}^*$. Namely,

$$i_{\gamma,D}^*(t) = i_\delta^*(t) \quad (55)$$

The generic description of a controller stage that corresponds to a filter stage of the power hardware was given in [4]. Let $\mathbf{K}_{FB,\lambda}$, $\mathbf{K}_{FF,\lambda}$, $\mathbf{K}_{FT,\lambda}$ be the proportional gains and $T_{FB,\lambda}$ the integration time of PI controller, respectively. The control law of an inductive filter stage is given by

$$\mathbf{v}_{\lambda-1,DQ}^* = \begin{bmatrix} \mathbf{K}_{FB,\lambda} \left(\Delta \mathbf{i}_{\lambda,DQ} + \frac{1}{T_{FB,\lambda}} \int \Delta \mathbf{i}_{\lambda,DQ} dt \right) \\ + \mathbf{K}_{FT,\lambda} \mathbf{v}_{\lambda+1,DQ} + \mathbf{K}_{FF,\lambda} \mathbf{i}_{\lambda,DQ}^* \end{bmatrix} \quad (56)$$

$$\Delta \mathbf{i}_{\lambda,DQ} := \mathbf{i}_{\lambda,DQ}^* - \mathbf{i}_{\lambda,DQ} \quad (57)$$

$\mathbf{v}_{\lambda-1,DQ}^*$, $\mathbf{i}_{\lambda,DQ}^*$ are the reference voltage at the input of the controller stage and the reference current at its output, respectively. $\mathbf{v}_{\lambda+1,DQ}$, $\mathbf{i}_{\lambda,DQ}$ are the voltage at the output of the filter stage and the current through it, respectively. The control

TABLE I
SHORT-CIRCUIT PARAMETERS OF THE THÉVENIN EQUIVALENT.

Parameter	Resource Validation	System Validation	Description
V_n	230 V-RMS	230 V-RMS	Nominal voltage
S_{sc}	267 kW	3.85 MW	Short-circuit power
$ Z_{sc} $	195 m Ω	13.7 m Ω	Short-circuit impedance
R_{sc}/X_{sc}	6.207	0.271	Resistance-to-reactance ratio

law for a capacitive filter stage is obtained analogously by replacing voltages with currents and vice versa.

Combining (55) with the equations of the controller stages from the AC and DC side, leads to the state-space model of the control software. As can be seen from Fig. 3 the control software is composed of PI controllers. Its state is then given by the temporal integrals of the errors w.r.t. the inductor currents $\Delta \mathbf{i}_{\alpha,DQ}$ and $\Delta \mathbf{i}_{\gamma,DQ}$, and the capacitor voltage $\Delta v_{\varphi,DQ}$. The input and output vectors are defined by the interconnection with the power hardware as shown in Fig. 3. The disturbance is the Q-component of the grid reference current $i_{\gamma,Q}^*$ and the DC-voltage reference V_δ^* . Accordingly

$$\mathbf{x}_\kappa(t) := \int \begin{bmatrix} \Delta \mathbf{i}_{\alpha,DQ}(t) \\ \Delta v_{\varphi,DQ}(t) \\ \Delta \mathbf{i}_{\gamma,DQ}(t) \\ \Delta v_\delta(t) \end{bmatrix} dt = \begin{bmatrix} \mathbf{x}_{\kappa,1}(t) \\ \mathbf{x}_{\kappa,2}(t) \\ \mathbf{x}_{\kappa,3}(t) \\ x_{\kappa,4}(t) \end{bmatrix} \quad (58)$$

$$\mathbf{u}_\kappa(t) := \begin{bmatrix} \mathbf{i}_{\alpha,DQ}(t) \\ v_{\varphi,DQ}(t) \\ \mathbf{i}_{\gamma,DQ}(t) \\ v_\delta(t) \\ v_{\gamma,DQ}(t) \\ i_\epsilon(t) \end{bmatrix} = \begin{bmatrix} \mathbf{u}_{\kappa,1}(t) \\ \mathbf{u}_{\kappa,2}(t) \\ \mathbf{u}_{\kappa,3}(t) \\ u_{\kappa,4}(t) \\ \mathbf{u}_{\kappa,5}(t) \\ u_{\kappa,6}(t) \end{bmatrix} \quad (59)$$

$$\mathbf{w}_\kappa(t) := \begin{bmatrix} i_{\gamma,Q}^*(t) \\ V_\delta^* \end{bmatrix} = \begin{bmatrix} w_{\kappa,1}(t) \\ w_{\kappa,2}(t) \end{bmatrix} \quad (60)$$

$$\mathbf{y}_\kappa(t) := \mathbf{v}_{\alpha,DQ}^*(t) \quad (61)$$

As opposed to the power hardware, the state-space model of the control software does purely depend on constant parameters, since no linearization needs to be performed. Therefore, all matrices can be directly described by (62)–(69). For the sake of clarity the following substitutions have been employed, $(K_{FF} + K_{FB}) = K_{FFB}$ and similarly $(\mathbf{K}_{FF} + \mathbf{K}_{FB}) = \mathbf{K}_{FFB}$.

In Fig. 3 the calculation of the Q-component of the grid reference current $i_{\gamma,Q}^*(t)$ is performed using the reactive power setpoint Q^* and the D-component of the grid voltage.

$$i_{\gamma,Q}^*(t) = \frac{Q^*}{v_{\gamma,D}(t)} \quad (70)$$

In [4] it is described how this reference calculation is incorporated in the HPF method.

V. VALIDATION OF THE RESOURCE MODEL

A. Methodology and Key Performance Indicators

The validation of the individual resource transfer function is performed using the test setup shown in Fig. 5. The CIDER is directly connected to a *Thévenin Equivalent* (TE), which is described by the short-circuit parameters given in Table I.

$$\tilde{\mathbf{A}}_{\kappa,0} = \begin{bmatrix} \mathbf{0}_{2 \times 2} & \frac{\mathbf{K}_{\text{FB},\varphi}}{T_{\text{FB},\varphi}} & \mathbf{K}_{\text{FFB},\varphi} \frac{\mathbf{K}_{\text{FB},\gamma}}{T_{\text{FB},\gamma}} & \mathbf{K}_{\text{FFB},\varphi} \mathbf{K}_{\text{FFB},\gamma} \mathbf{e}_1 \frac{K_{\text{FB},\delta}}{T_{\text{FB},\delta}} \\ \mathbf{0}_{2 \times 2} & \mathbf{0}_{2 \times 2} & \frac{\mathbf{K}_{\text{FB},\gamma}}{T_{\text{FB},\gamma}} & \mathbf{K}_{\text{FFB},\gamma} \mathbf{e}_1 \frac{K_{\text{FB},\delta}}{T_{\text{FB},\delta}} \\ \mathbf{0}_{1 \times 2} & \mathbf{0}_{1 \times 2} & \mathbf{0}_{1 \times 2} & \frac{K_{\text{FB},\delta}}{T_{\text{FB},\delta}} \\ \mathbf{0}_{1 \times 2} & \mathbf{0}_{1 \times 2} & \mathbf{0}_{1 \times 2} & 0 \\ \mathbf{0}_{1 \times 2} & \mathbf{0}_{1 \times 2} & \mathbf{0}_{1 \times 2} & 0 \end{bmatrix} \quad (62)$$

$$\tilde{\mathbf{B}}_{\kappa,0} = \begin{bmatrix} -\text{diag}(\mathbf{1}_2) & -\mathbf{K}_{\text{FB},\varphi} & \mathbf{K}_{\text{FT},\varphi} & -\mathbf{K}_{\text{FFB},\varphi} \mathbf{K}_{\text{FB},\gamma} & -\mathbf{K}_{\text{FFB},\varphi} \mathbf{K}_{\text{FFB},\gamma} \mathbf{e}_1 K_{\text{FB},\delta} & \mathbf{K}_{\text{FFB},\varphi} \mathbf{K}_{\text{FT},\gamma} & \mathbf{K}_{\text{FFB},\varphi} \mathbf{K}_{\text{FFB},\gamma} \mathbf{e}_1 K_{\text{FT},\delta} \\ \mathbf{0}_{2 \times 2} & -\text{diag}(\mathbf{1}_2) & & -\mathbf{K}_{\text{FB},\gamma} & -\mathbf{K}_{\text{FFB},\gamma} \mathbf{e}_1 K_{\text{FB},\delta} & \mathbf{K}_{\text{FT},\gamma} & \mathbf{K}_{\text{FFB},\gamma} \mathbf{e}_1 K_{\text{FT},\delta} \\ \mathbf{0}_{1 \times 2} & \mathbf{0}_{1 \times 2} & & -\mathbf{e}_1^\top & -K_{\text{FB},\delta} & \mathbf{0}_{1 \times 2} & K_{\text{FT},\delta} \\ \mathbf{0}_{1 \times 2} & \mathbf{0}_{1 \times 2} & & -\mathbf{e}_2^\top & 0 & \mathbf{0}_{1 \times 2} & 0 \\ \mathbf{0}_{1 \times 2} & \mathbf{0}_{1 \times 2} & & \mathbf{0}_{1 \times 2} & -1 & \mathbf{0}_{1 \times 2} & 0 \end{bmatrix} \quad (63)$$

$$\tilde{\mathbf{E}}_{\kappa,0} = \begin{bmatrix} \mathbf{K}_{\text{FFB},\varphi} \mathbf{K}_{\text{FFB},\gamma} \mathbf{e}_2 & \mathbf{K}_{\text{FFB},\varphi} \mathbf{K}_{\text{FFB},\gamma} \mathbf{e}_1 K_{\text{FFB},\delta} \\ \mathbf{K}_{\text{FFB},\gamma} \mathbf{e}_2 & \mathbf{K}_{\text{FFB},\gamma} \mathbf{e}_1 K_{\text{FFB},\delta} \\ 0 & K_{\text{FFB},\delta} \\ 1 & 0 \\ 0 & 1 \end{bmatrix} \quad (64)$$

$$\tilde{\mathbf{C}}_{\kappa,0} = \begin{bmatrix} \frac{K_{\text{FB},\alpha}}{T_{\text{FB},\alpha}} & \mathbf{K}_{\text{FFB},\alpha} \frac{\mathbf{K}_{\text{FB},\varphi}}{T_{\text{FB},\varphi}} & \mathbf{K}_{\text{FFB},\alpha} \mathbf{K}_{\text{FFB},\varphi} \mathbf{K}_{\text{FFB},\gamma} & \mathbf{K}_{\text{FFB},\alpha} \mathbf{K}_{\text{FFB},\varphi} \mathbf{K}_{\text{FFB},\gamma} \mathbf{e}_1 \frac{K_{\text{FB},\delta}}{T_{\text{FB},\delta}} \end{bmatrix} \quad (65)$$

$$\tilde{\mathbf{D}}_{\kappa,0} = \begin{bmatrix} -\mathbf{K}_{\text{FB},\alpha} & \mathbf{K}_{\text{FT},\alpha} & -\mathbf{K}_{\text{FFB},\alpha} \mathbf{K}_{\text{FB},\varphi} & (\tilde{\mathbf{D}}_{\kappa,0})_3 & (\tilde{\mathbf{D}}_{\kappa,0})_4 & \mathbf{K}_{\text{FFB},\alpha} \mathbf{K}_{\text{FFB},\varphi} \mathbf{K}_{\text{FT},\gamma} & \mathbf{K}_{\text{FFB},\alpha} \mathbf{K}_{\text{FFB},\varphi} \mathbf{K}_{\text{FFB},\gamma} \mathbf{e}_1 K_{\text{FT},\delta} \end{bmatrix} \quad (66)$$

$$(\tilde{\mathbf{D}}_{\kappa,0})_3 = \mathbf{K}_{\text{FFB},\alpha} (\mathbf{K}_{\text{FT},\varphi} - \mathbf{K}_{\text{FFB},\varphi} \mathbf{K}_{\text{FB},\gamma}) \quad (67)$$

$$(\tilde{\mathbf{D}}_{\kappa,0})_4 = -\mathbf{K}_{\text{FFB},\alpha} \mathbf{K}_{\text{FFB},\varphi} \mathbf{K}_{\text{FFB},\gamma} \mathbf{e}_1 K_{\text{FB},\delta} \quad (68)$$

$$\tilde{\mathbf{F}}_{\kappa,0} = \begin{bmatrix} \mathbf{K}_{\text{FFB},\alpha} \mathbf{K}_{\text{FFB},\varphi} \mathbf{K}_{\text{FFB},\gamma} \mathbf{e}_2 & \mathbf{K}_{\text{FFB},\alpha} \mathbf{K}_{\text{FFB},\varphi} \mathbf{K}_{\text{FFB},\gamma} \mathbf{e}_1 K_{\text{FFB},\delta} \end{bmatrix} \quad (69)$$

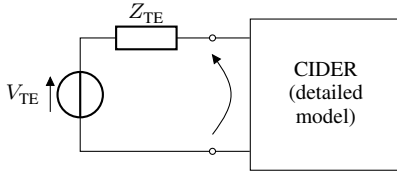


Fig. 5. Test setup for the validation of the HPF method on individual CIDERs. The resource is represented by a detailed state-space model (see Section IV), and the power system by a Thévenin equivalent (see Tables I and II).

TABLE II
HARMONIC VOLTAGES OF THE THÉVENIN EQUIVALENT (SEE [18]).

h	$ V_{\text{TE},h} $	$\angle V_{\text{TE},h}$
1	1.0 p.u.	0.00 deg
5	6.0 %	0.00 deg
7	5.0 %	0.00 deg
11	3.5 %	0.00 deg
13	3.0 %	0.00 deg
17	2.0 %	0.00 deg
19	1.5 %	0.00 deg
23	1.5 %	0.00 deg

Furthermore, the TE injects harmonics with levels shown in Table II based on [18]. The angles are set in order to achieve significant harmonics on the DC side.

The parameters of the grid-following CIDER that includes the DC-side characteristics are given in Table III. The parameters of the AC-filter and the DC-link capacitor are derived based on the design guidelines proposed in [19]. The active and reactive power setpoints are $P^* = 50$ kW and $Q^* = 16.4$ kVAR, respectively, and $V_\delta^* = 900$ V.

TABLE III
PARAMETERS OF THE GRID-FOLLOWING RESOURCE
(RATED POWER 60 kVA).

Filter stage	L/C	R/G	K_{FB}	T_{FB}	K_{FT}
DC-Link Capacitor (δ)	310 μF	0 S	10	3e-3	1
Actuator-side inductor (α)	325 μH	1.02 m Ω	9.56	1.47e-4	1
Capacitor (φ)	90.3 μF	0 S	0.569	8.97e-4	0
Grid-side inductor (γ)	325 μH	1.02 m Ω	0.23	1e-3	1

In the context of this paper the Matlab project of the HPF method proposed in [3], [4] is extended to include the DC-side modelling. As comparison *Time-Domain Simulations* (TDS) in Simulink are conducted using averaged models of the CIDERs. Additionally, the Simulink models are updated to include the DC-side characteristics. A *Discrete Fourier Transform* (DFT) of the last 5 periods of the fundamental frequency in steady state is performed. All signals are normalized w.r.t. the base power $P_b = 50$ kW and the base voltage $V_b = 230$ V-RMS.

In order to assess the accuracy of the HPF method *Key Performance Indicators* (KPIs) are defined. That is, the accuracy is defined as the errors of the harmonic phasors between the DFT of the TDS and the results of the HPF. If the Fourier coefficient of a three-phase electrical quantity (i.e., voltage or current) is denoted as \mathbf{X}_h , the KPIs are defined as follows:

$$e_{\text{abs}}(\mathbf{X}_h) := \max_p \left| |X_{h,p,HPF}| - |X_{h,p,TDS}| \right| \quad (71)$$

$$e_{\text{arg}}(\mathbf{X}_h) := \max_p \left| \angle X_{h,p,HPF} - \angle X_{h,p,TDS} \right| \quad (72)$$

In other words, $e_{\text{abs}}(\mathbf{X}_h)$ and $e_{\text{arg}}(\mathbf{X}_h)$ describe the maximum absolute errors over all phases $p \in \mathcal{P}$ in magnitude and phase, respectively.

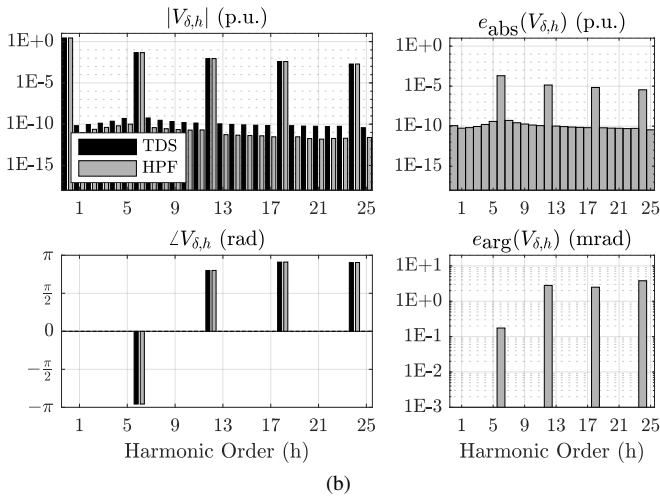
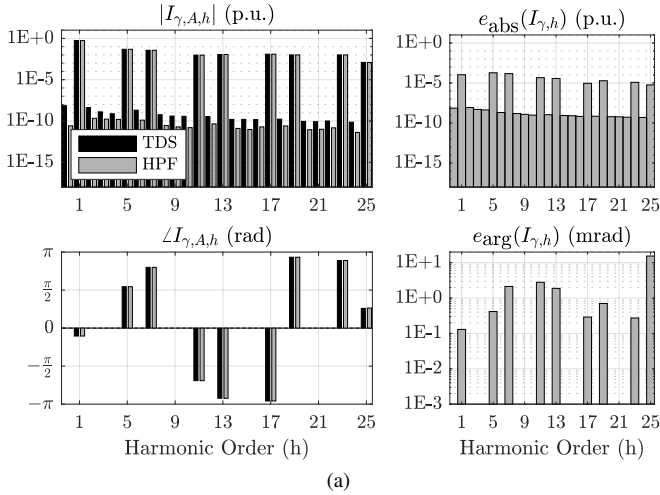


Fig. 6. Results of the validation on individual grid-following CIDER. The grid current (6a) and DC-side voltage (6b) are shown. The plots on the left-hand side show the spectra (i.e., for phase A in case of the grid current), and the ones on the right-hand side the error defined through the KPIs.

B. Results and Discussion

In Fig. 6 the results for the controlled quantities (i.e., the grid-current and the DC-link voltage) of the individual CIDER is shown. The left-hand side of the plots depict the magnitude and angle of the Fourier coefficients obtained with the HPF and TDS, respectively. The quantities are almost identically, yielding small KPIs as shown on the right-hand side of the plots. The highest errors are $e_{\text{abs}}(\mathbf{I}_{\gamma,5}) = 1.88\text{E-}4$ p.u. and $e_{\text{arg}}(\mathbf{I}_{\gamma,25}) = 15.5$ mrad for the grid current and $e_{\text{abs}}(\mathbf{V}_{\delta,6}) = 2.02\text{E-}4$ p.u. and $e_{\text{arg}}(\mathbf{V}_{\delta,24}) = 3.8$ mrad for the DC-link voltage. Notably, since the applied TE voltage does not include unbalances, the DC-link voltage exhibits only even harmonics.

VI. VALIDATION OF THE EXTENDED ALGORITHM

A. Methodology and Key Performance Indicators

The extension of the HPF algorithm that includes the DC side of the CIDERs is validated on a test system adapted from CIGRÉ low-voltage benchmark microgrid [20]. It is composed of a substation at node N1, five grid-following CIDERs at nodes N11, and N15-N18 and four unbalanced loads at

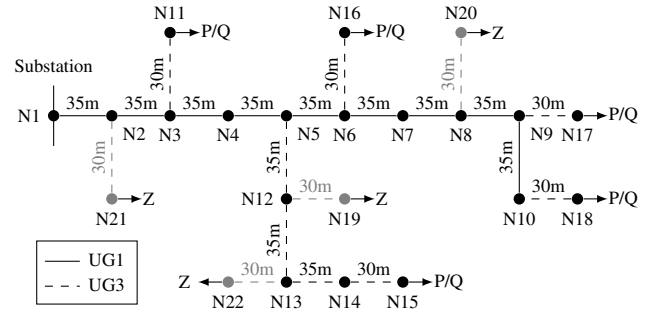


Fig. 7. Schematic diagram of the test system, which is based on the CIGRÉ low-voltage benchmark microgrid [20] (in black) and extended by unbalanced impedance loads (in grey). For the cable parameters see Table IV. The set of grid-following resources are composed of constant impedance loads (Z) and constant power loads (P/Q), their parameters are given in Table V.

TABLE IV
SEQUENCE PARAMETERS OF THE LINES IN THE TEST SYSTEM.

ID	R_+/R_-	R_0	L_+/L_-	L_0	C_+/C_-	C_0
UG1	0.162 Ω	0.529 Ω	0.262 mH	1.185 mH	637 nF	388 nF
UG3	0.822 Ω	1.794 Ω	0.270 mH	3.895 mH	637 nF	388 nF

nodes N19-N22. The feeding substation is modelled as a TE described by parameters depicted in Table I. The TE injects harmonics with the same parameters as for the validation in Section V-A (i.e., see Table II). Notably, these parameters account for both the substation transformer and the upstream grid. The lines are described by the sequence parameters given in Table IV. The parameters of the grid-following CIDERs are identical to the ones used in the individual resource validation (i.e., they are given in Table III). Unbalances are introduced into the grid through the unbalanced wye-connected constant-impedance loads at nodes N19-N22. The amount of unbalance is expressed by phase weights, that describe the distribution of the load over the phases. All setpoints and phase weights of the grid-following resources are given in Table V.

The Newton-Raphson algorithm is initialized as described in Section III. That is, initial values of AC and DC quantities are based on balanced, sinusoidal conditions and nominal values or setpoints. In order to assess the robustness of the convergence, this initial point is distorted with random positive, negative and homopolar sequence components. The magnitudes and phases are chosen from uniform distributions within $\pm 20\%$ and $[0, 2\pi)$, respectively. The accuracy of the result is assessed using the same KPIs as for the validation of the individual resource model.

B. Results and Discussion

The accuracy of the HPF method including the DC-side characteristics is shown in Fig. 8. The highest errors at every harmonic frequency and over all nodes and phases are shown. The maximum errors regarding the voltage in magnitude and angle are $e_{\text{abs}}(\mathbf{V}_7) = 7.86\text{E-}5$ p.u. and $e_{\text{arg}}(\mathbf{V}_{25}) = 16.1$ mrad, respectively. In terms of errors w.r.t. current magnitude and angle the highest values are $e_{\text{abs}}(\mathbf{I}_1) = 3.1\text{E-}4$ p.u. and $e_{\text{arg}}(\mathbf{I}_{25}) = 22.0$ mrad, respectively. Notably, the observed

TABLE V
PARAMETERS OF THE GRID-FOLLOWING RESOURCES AND LOADS
IN THE TEST SYSTEM.

Node	S	pf	Type	Phase weights
N11	15.0 kW	0.95	P/Q	[0.33 0.33 0.33]
N15	52.0 kW	0.95	P/Q	[0.33 0.33 0.33]
N16	55.0 kW	0.95	P/Q	[0.33 0.33 0.33]
N17	35.0 kW	0.95	P/Q	[0.33 0.33 0.33]
N18	47.0 kW	0.95	P/Q	[0.33 0.33 0.33]
N19	-51.2 kW	0.95	Z	[0.31 0.50 0.19]
N20	-51.7 kW	0.95	Z	[0.45 0.23 0.32]
N21	-61.5 kW	0.95	Z	[0.24 0.39 0.37]
N22	-61.9 kW	0.95	Z	[0.31 0.56 0.13]

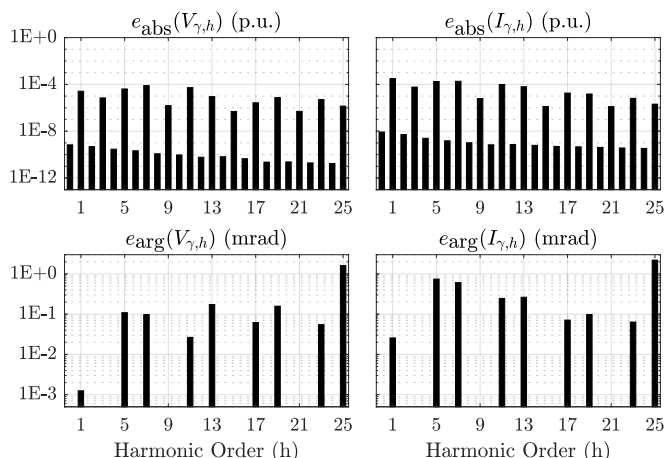


Fig. 8. Results of the validation on the benchmark system for the grid-following CIDERS. The plots show the maximum absolute errors over all nodes and phases, for voltages (left column) and currents (right column), in magnitude (top row) and phase (bottom row).

errors are very low, i.e., lower than the accuracy of standard measurement devices.

VII. CONCLUSIONS

This paper proposes an extension for the HPF study of three-phase power grids with CIDERS introduced in [3], [4]. More specifically, it is shown in this paper how the DC-side of a CIDER is included into the CIDER model and the HPF study. The DC side is represented by the current-source model together with the DC-link capacitor and is connected to the AC side through an AC/DC converter. Including the latter into the CIDER model introduces a nonlinearity that needs to be approximated for the numerical solution of HPF study. To this end, it is shown how nonlinearities within the internal structure of the CIDER can be linearized and incorporated into the HPF algorithm. In particular, the linearization takes into account the entire harmonic content of a signal, as opposed to the fundamental component only. The extended HPF method allows to study AC/DC and converter interactions in a power system. The validation of the individual CIDER model confirms that the linearization is indeed accurate. The validation of the extended algorithm is performed on an entire system (i.e., the CIGRÉ low-voltage benchmark microgrid), and provides high precisions too. The largest observed errors are $3.1E-4$ p.u. w.r.t.

current magnitude, $7.86E-5$ p.u. w.r.t. voltage magnitude, and 22 mrad w.r.t. phase. These findings show that it is possible to accurately analyze AC/DC and converter interactions using the extended HPF method proposed in this paper.

REFERENCES

- [1] J. Enslin and P. Heskes, "Harmonic interaction between a large number of distributed power inverters and the distribution network," *IEEE Trans. Power Electron.*, vol. 19, no. 6, pp. 1586–1593, 2004.
- [2] T. Friedli, M. Hartmann, and J. W. Kolar, "The essence of three-phase pfc rectifier systems—part ii," *IEEE Trans. Power Electron.*, vol. 29, no. 2, pp. 543–560, 2013.
- [3] A. M. Kettner, L. Reyes-Chamorro, J. K. M. Becker, Z. Zou, M. Liserre, and M. Paolone, "Harmonic power-flow study of polyphase grids with converter-interfaced distributed energy resources—part i: Modeling framework and algorithm," *IEEE Transactions on Smart Grid*, vol. 13, no. 1, pp. 458–469, 2021.
- [4] J. K. M. Becker, A. M. Kettner, L. Reyes-Chamorro, Z. Zou, M. Liserre, and M. Paolone, "Harmonic power-flow study of polyphase grids with converter-interfaced distributed energy resources—part ii: Model library and validation," *IEEE Transactions on Smart Grid*, vol. 13, no. 1, pp. 470–481, 2021.
- [5] G. De Carne, G. Lauss, M. H. Syed, A. Monti, A. Benigni, S. Karrari, P. Kotsampopoulos, and M. O. Faruque, "On modeling depths of power electronic circuits for real-time simulation—a comparative analysis for power systems," *IEEE Open Access Journal of Power and Energy*, vol. 9, pp. 76–87, 2022.
- [6] T.-F. Wu, C.-H. Chang, L.-C. Lin, and C.-L. Kuo, "Power loss comparison of single-and two-stage grid-connected photovoltaic systems," *IEEE Transactions on Energy Conversion*, vol. 26, no. 2, pp. 707–715, 2011.
- [7] S. B. Kjaer, J. K. Pedersen, and F. Blaabjerg, "A review of single-phase grid-connected inverters for photovoltaic modules," *IEEE transactions on industry applications*, vol. 41, no. 5, pp. 1292–1306, 2005.
- [8] F. Blaabjerg, Z. Chen, and S. B. Kjaer, "Power electronics as efficient interface in dispersed power generation systems," *IEEE transactions on power electronics*, vol. 19, no. 5, pp. 1184–1194, 2004.
- [9] D. Lu, X. Wang, and F. Blaabjerg, "Impedance-based analysis of dc-link voltage dynamics in voltage-source converters," *IEEE Transactions on Power Electronics*, vol. 34, no. 4, pp. 3973–3985, 2018.
- [10] B. Gao, Y. Wang, and W. Xu, "An improved model of voltage source converters for power system harmonic studies," *IEEE Transactions on Power Delivery*, 2021.
- [11] J. Kwon, X. Wang, F. Blaabjerg, C. L. Bak, V.-S. Sularea, and C. Busca, "Harmonic interaction analysis in a grid-connected converter using harmonic state-space (hss) modeling," *IEEE Transactions on Power Electronics*, vol. 32, no. 9, pp. 6823–6835, 2016.
- [12] M. Cespedes and J. Sun, "Impedance modeling and analysis of grid-connected voltage-source converters," *IEEE Transactions on Power Electronics*, vol. 29, no. 3, pp. 1254–1261, 2013.
- [13] A. Rygg, M. Molinas, C. Zhang, and X. Cai, "On the equivalence and impact on stability of impedance modeling of power electronic converters in different domains," *IEEE Journal of Emerging and Selected Topics in Power Electronics*, vol. 5, no. 4, pp. 1444–1454, 2017.
- [14] N. Pogaku, M. Prodanovic, and T. C. Green, "Modeling, analysis and testing of autonomous operation of an inverter-based microgrid," *IEEE Transactions on power electronics*, vol. 22, no. 2, pp. 613–625, 2007.
- [15] N. M. Wereley, "Analysis and control of linear periodically time-varying systems," Ph.D. dissertation, MIT, Cambridge, MA, USA, 1991.
- [16] X. Wang and F. Blaabjerg, "Harmonic stability in power electronic-based power systems: Concept, modeling, and analysis," *IEEE Transactions on Smart Grid*, vol. 10, no. 3, pp. 2858–2870, 2018.
- [17] J. Peralta Rodriguez, "Dynamic averaged models of vsc-based hvdc systems for electromagnetic transient programs," Ph.D. dissertation, École Polytechnique de Montréal, 2013.
- [18] "Voltage characteristics of electricity supplied by public distribution networks," British Standards Institution, London, UK, Std. BS-EN-50160:2000, 2000.
- [19] M. Liserre, F. Blaabjerg, and A. Dell'Aquila, "Step-by-step design procedure for a grid-connected three-phase pwm voltage source converter," *International journal of electronics*, vol. 91, no. 8, pp. 445–460, 2004.
- [20] K. Strunz *et al.*, "Benchmark systems for network integration of renewable and distributed energy resources," CIGRÉ, Paris, IDF, FR, Tech. Rep. 575, 2014.